Journal of Materials Chemistry B

ROYAL SOCIETY OF CHEMISTRY

PAPER

View Article Online
View Journal | View Issue

Cite this: J. Mater. Chem. B, 2025, 13, 11750

A near-infrared light absorbable hydrogel with antibacterial effect for mild photothermal regeneration of infected wounds

Kiyan Musaie,†[a] Mostafa Qahremani,†[b] Shima Ebadi,[b] Hooman Haghighi,[b] Vahideh Nosrati Siahmazgi,[b] Samin Abbaszadeh,[c] Mohammad Reza Eskandari,[d] Marja Slomp,[a] Jelly Atema-Smit,[a] Hélder A. Santos *[a] and Mohammad-Ali Shahbazi *[a]

Bacterial wounds are currently a growing concern in clinical practice, with the rising challenge posed by antibiotic resistance and inflammation. Traditional photothermal therapy (PTT) presents great efficiency in treating infected wounds; however, it has the limitation of thermal damage to healthy tissues. To overcome this challenge, the strategy of mild-PTT is proposed using hyaluronic acid-coated bismuth sulfide (Bi_2S_3) nanoparticles (BiH NPs) alongside allantoin within gelatin/sodium alginate-based hydrogel formulation to eliminate bacterial infections and facilitate the wound healing procedure. BiH NP as a photothermal agent is synthesized *via* a facile and environmentally friendly method with excellent biocompatibility and high photothermal efficiency. Our formulation demonstrated good mechanical resistance with high recoverable compressibility and favorable bactericidal effects on *Escherichia coli* and *Staphylococcus aureus* bacteria. Moreover, as a multifunctional system, it accelerates wound healing in non-infected and infected full-thickness wound models with desirable *in vitro* and *in vivo* biocompatibility. With the simple preparation procedure, potent antibacterial effect, and high photothermal efficiency, this hydrogel emerges as a promising candidate for the treatment of infected wounds.

Received 5th June 2025,
Accepted 17th August 2025

DOI: 10.1039/d5tb01346a

rsc.li/materials-b

1. Introduction

Skin, the first barrier of the immune system, supports internal organs against threatening factors; however, it is exposed to injury due to different reasons such as trauma, surgery, skin disease, diabetes, and burns.[1,2] Although most skin damages recover in a short time, complex wounds like infected wounds have an extended inflammation phase, causing sepsis, swelling, pain, and redness. Currently, antibiotic therapy is the common way to deal with bacterial infection. Unfortunately, indiscriminate and irrational consumption of antibiotics has led to the emergence of multiple drug-resistant bacteria.[3] Therefore, the development of efficient and on-time treatment is critical to minimize the possibility of bacterial infection to promote wound repair.

In recent years, photothermal therapy (PTT), which converts near-infrared (NIR) light into heat, has been investigated for its broad-spectrum antibacterial potential due to its ability to increase bacterial membrane permeability and induce protein denaturation.[4] NIR laser alone is safe for healthy biological tissues, as it has low absorbance and high light scattering in biological media. However, elevated local temperature (55–60 °C) poses challenges to normal tissue integrity. To avoid this limitation, mild-photothermal therapy (m-PTT) utilizing lower temperatures (<45 °C) in synergy with bioactive antibacterial agents has been offered as a new strategy to address the intricate needs of infectious wounds.[5,6] In this line, the usage of traditional photoactive nanomaterials like gold nanoparticles and carbon-based nanoparticles is limited due to the cost and lower absorption of NIR irradiation, respectively.[7] Instead, bismuth sulfide (Bi_2S_3) nanoparticles showed high PTT performance[8] and high biocompatibility,[9] as well as antibacterial activity against *Escherichia coli* (*E. coli*)[10,11] and *Staphylococcus aureus* (*S. aureus*)[10] bacteria.

[a] Department of Biomaterials and Biomedical Technology, The Personalized Medicine Research Institute (PRECISION), University Medical Center Groningen, University of Groningen, 9713 AV Groningen, The Netherlands. E-mail: h.a.santos@umcg.nl, m.a.shahbazi@umcg.nl
[b] Department of Pharmaceutical Biomaterials, School of Pharmacy, Zanjan University of Medical Science, 45139-56184 Zanjan, Iran
[c] Department of Pharmacology and Toxicology, Faculty of Pharmacy, Urmia University of Medical Sciences, 57561-15327 Urmia, Iran
[d] Department of Pharmacology and Toxicology, School of Pharmacy, Zanjan University of Medical Science, 45139-56184 Zanjan, Iran
† These authors equally contributed to the present work.

In addition, incorporation of photoactive agents within a hydrogel network can further minimize the adverse effects of PTT by producing predictable and even heat generation and avoiding uncontrolled hot spots in wound tissue.[12] Hydrogels with their desirable biocompatibility, moisture regulation properties, and controlled release of active pharmaceutical ingredients are favorable carriers for wound healing applications.[13] Gelatin (G), a protein derived from collagen, and sodium alginate (A), an anionic polysaccharide, both offer abundant functional groups (*e.g.*, hydroxyl, primary amine, and carboxyl groups) that enable chemical crosslinking with genipin,[14,15] poly(ethylene glycol) diglycidyl ether (PEGDGE),[16,17] and Fe^{3+}.[18]

Herein, hyaluronic acid-coated Bi_2S_3 NPs (BiH NPs) and allantoin (Al) are co-loaded in a gelatin-sodium alginate (GA) hydrogel crosslinked by PEGDGE to develop GA–Al–BiH hydrogel (Fig. 1a). Al, as a pharmaceutically active ingredient, has been reported to have an antibacterial effect against *S. aureus*, *E. coli*, and *Pseudomonas aeruginosa*,[19] as well as skin cell regeneration properties owing to the induction of fibroblast proliferation.[20] BiH NPs with excellent m-PTT performance can

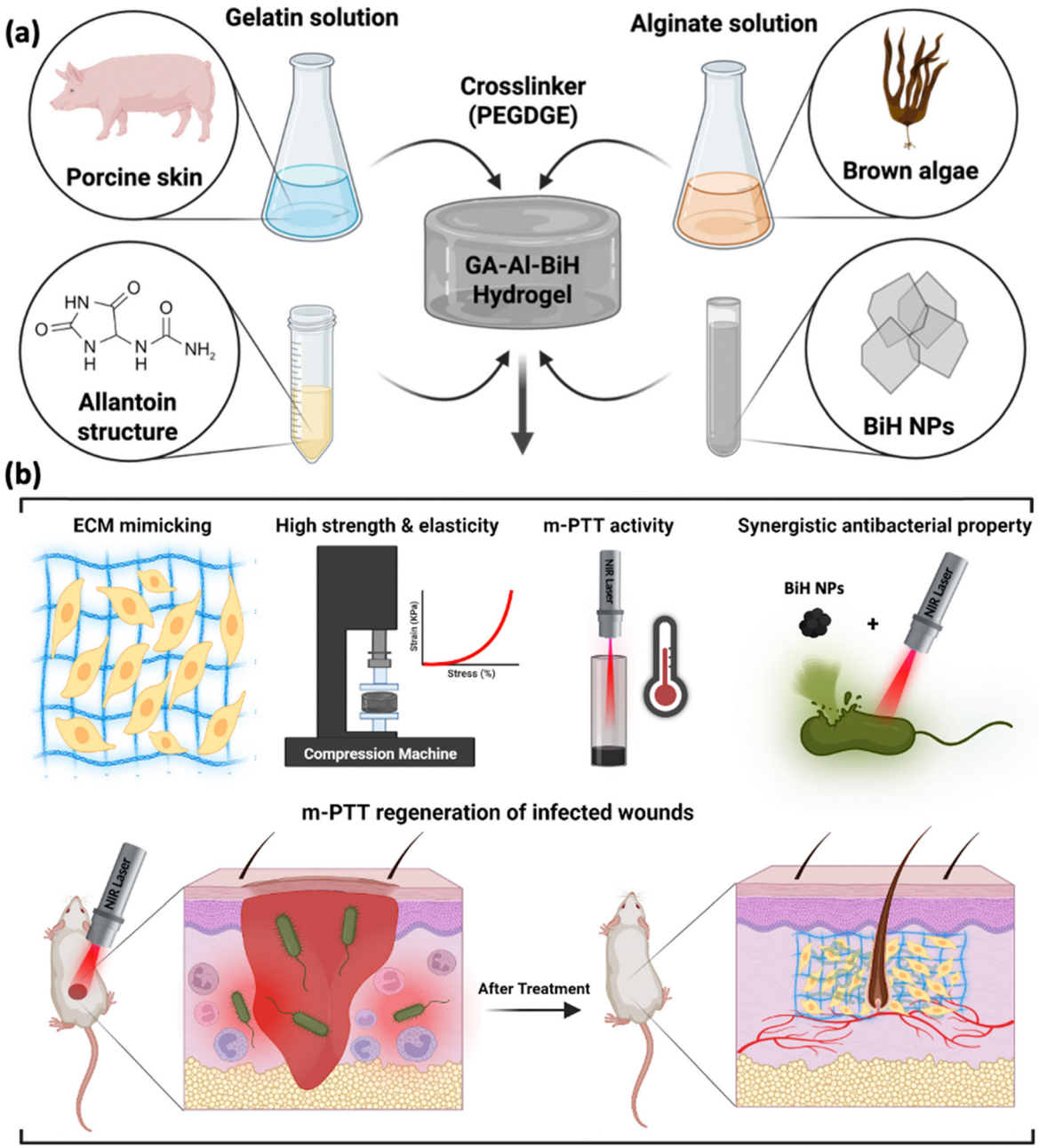

Fig. 1 Schematic illustration of the preparation procedure of the GA–Al–BiH hydrogel and the expected functions of the hydrogel. (a) The components of the injectable hydrogel crosslinked by PEGDGE and the incorporation of the BiH NPs and Al. (b) The prepared system displays multifunctional activity, including ECM mimicking, great mechanical properties, photothermal effect, and antibacterial activity for infected wound healing. The picture is created in https://Biorender.com.

be used to eliminate bacterial infection and protect the wound area from secondary infections during the treatment procedure. While gelatin offers signal peptides like Arg–Gly–Asp (RGD), alginate provides the desirable hydration and porosity to the hydrogel structure, together creating a balanced extracellular matrix (ECM)-mimicking platform. ECM plays a key role in wound tissue for structural support, cellular attachment, and regulating biochemical and biomechanical signaling pathways. Thus, a multifunctional GA–Al–BiH hydrogel with m-PTT performance is expected to be a good candidate for accelerating the healing process of normal and infectious wounds (Fig. 1b).

2. Results & discussion

2.1. Synthesis and physicochemical characterization of NPs

BiH NPs were synthesized by a facile fabrication method in several consecutive steps, as represented in Fig. 2a. In an environmentally friendly approach, $Bi(NO_3)_3{\cdot}5H_2O$ with L-cysteine formed different early precursor complexes such as $[Bi(L\text{-cysteine})_2]^{3+}$.[21] Then, the formed complexes were turned into Bi_2S_3 NPs in alkaline conditions, resulting in a color change from colorless to black after stirring at 78 °C for 24 h. Next, the obtained NPs were coated with HA under sonication to obtain BiH NPs.

Moreover, the physicochemical properties of the NPs were studied to prove the successful synthesis procedure. Transmission electron microscopy (TEM) images revealed that BiH NPs possess a nanosheet-like morphology (Fig. 2b). Their ultrathin structure and high specific surface area enable a rapid response to external stimuli such as light, resulting in high photothermal efficiency. In addition, the energy-dispersive X-ray spectroscopy (EDAX) spectrum and elemental mapping of BiH NPs revealed the uniform dispersion and presence of bismuth, sulfur, carbon, and oxygen elements with weight percentages of 68.3%, 10.1%, 12.4%, and 9.1%, respectively (Fig. 2c and d). The presence of oxygen and carbon elements corresponded to a successful coating process by HA. Furthermore, X-ray photoelectron spectroscopy (XPS) results showed symmetric Bi 4f peaks with well-separated spin–orbit components (Δ = 5.3 eV), indicating the presence of bismuth compounds, such as Bi_2S_3, instead of bismuth metal (Fig. 2e and f). The high-resolution Bi 4f spectra showed two predominant peaks at 158.45 eV and 163.75 eV corresponding to the spin state of Bi $4f_{7/2}$ and Bi $4f_{5/2}$, respectively, indicating the energy binding state of Bi^{3+}.[22] These peaks were shifted from the metallic bismuth peak at 156.95 eV. The low intensity of this peak suggested that the zero oxidation state of the Bi is a minor component.

2.2. Preparation of hydrogels

The gelation process of hydrogels was evaluated with the "flowability under heat" method.[23] Due to the sol–gel conversion of gelatin at room temperature, the macroscopic behavior of hydrogels was investigated at higher temperatures to confirm the successful crosslinking and gel formation. As shown in Fig. 3a, the GA mixture was prepared with two different proportions of G to A (1 : 1 and 4.5 : 1) with and without PEGDGE as a crosslinker and studied in two neutral and basic environments. Initially, all the samples were solidified at room temperature due to the presence of gelatin. At neutral pH, both crosslinked and non-crosslinked GA samples showed low viscosity and even solution behavior when exposed to heat in a water bath, owing to weak connections between the components of the mixtures. However, the GA hydrogel represented no flow at alkaline pH when subjected to high temperatures. In the alkaline condition, the nucleophilic groups of gelatin and sodium alginate, like amino and carboxyl groups, were deprotonated and amplified to attack the epoxy ring in PEGDGE, resulting in epoxy ring opening, and subsequently, establishing chemical crosslinking.[24] Moreover, adding BiH NPs in the GA mixtures did not interfere with the gelation process at the alkaline condition.

2.3. Characterization of hydrogels

2.3.1. Initial water content (IWC) and yield. The IWC of GA(1 : 1), GA(1 : 1)–BiH, GA(4.5 : 1), and GA(4.5 : 1)–BiH hydrogels were more than 90%, suggesting the high amount of water molecules entrapped in the pores of hydrogels (Fig. 3b). Furthermore, the yield value of all prepared hydrogels was more than 75% (Fig. 3c). In addition, the usage of different concentrations of polymers or the incorporation of the BiH NPs did not interfere with the IWC and yield rates.

2.3.2. Gel content, water retention, and non-degraded hydrogel ratio. One of the macroscopic indicators for investigating the interactions between hydrogel components is the gel content. The gel content of GA(4.5 : 1) and GA(4.5 : 1)–BiH hydrogels were significantly higher than GA(1 : 1) and GA(1 : 1)–BiH hydrogels, confirming the increased ratio of gelatin to sodium alginate enhances the efficiency of gel formation and enhanced binding among functional groups of the polymers (Fig. 3d), which correlates with better hydrogel strength and mechanical property.[25] Moreover, high water retention is another fundamental parameter for the design of wound dressings by providing a moist environment to absorb the wound extrudes, facilitating cell growth, angiogenesis, fibrinolysis, and preventing scar formation.[26] The amount of remaining water in the GA(4.5 : 1) and GA(4.5 : 1)–BiH hydrogels was higher than GA(1 : 1) and GA(1 : 1)–BiH hydrogels after 24 h at room temperature (Fig. 3e). A higher ratio of gelatin to sodium alginate provides stronger connections of polymer chains in hydrogels, which results in a high quantity of water in the three-dimensional structure of the hydrogel for longer hours. Furthermore, the high durability of the dressing platform is a notable feature that facilitates the controlled and prolonged release of drug and ECM-mimicking material to the wound site. Non-degraded hydrogel ratio demonstrated that GA(1 : 1), GA(1 : 1)–BiH, GA(4.5 : 1), and GA(4.5 : 1)–BiH hydrogels did not degrade completely in two weeks (Fig. 3f). The degradation rate of all hydrogels in the early hours was higher compared to subsequent hours. Furthermore, in all time points, the percentage of degradation for GA(4.5 : 1) and GA(4.5 : 1)–BiH hydrogels was less than GA(1 : 1) and GA(1 : 1)–BiH hydrogels. Hydrogels with a higher amount of gelatin in the hydrogel matrix have a lower

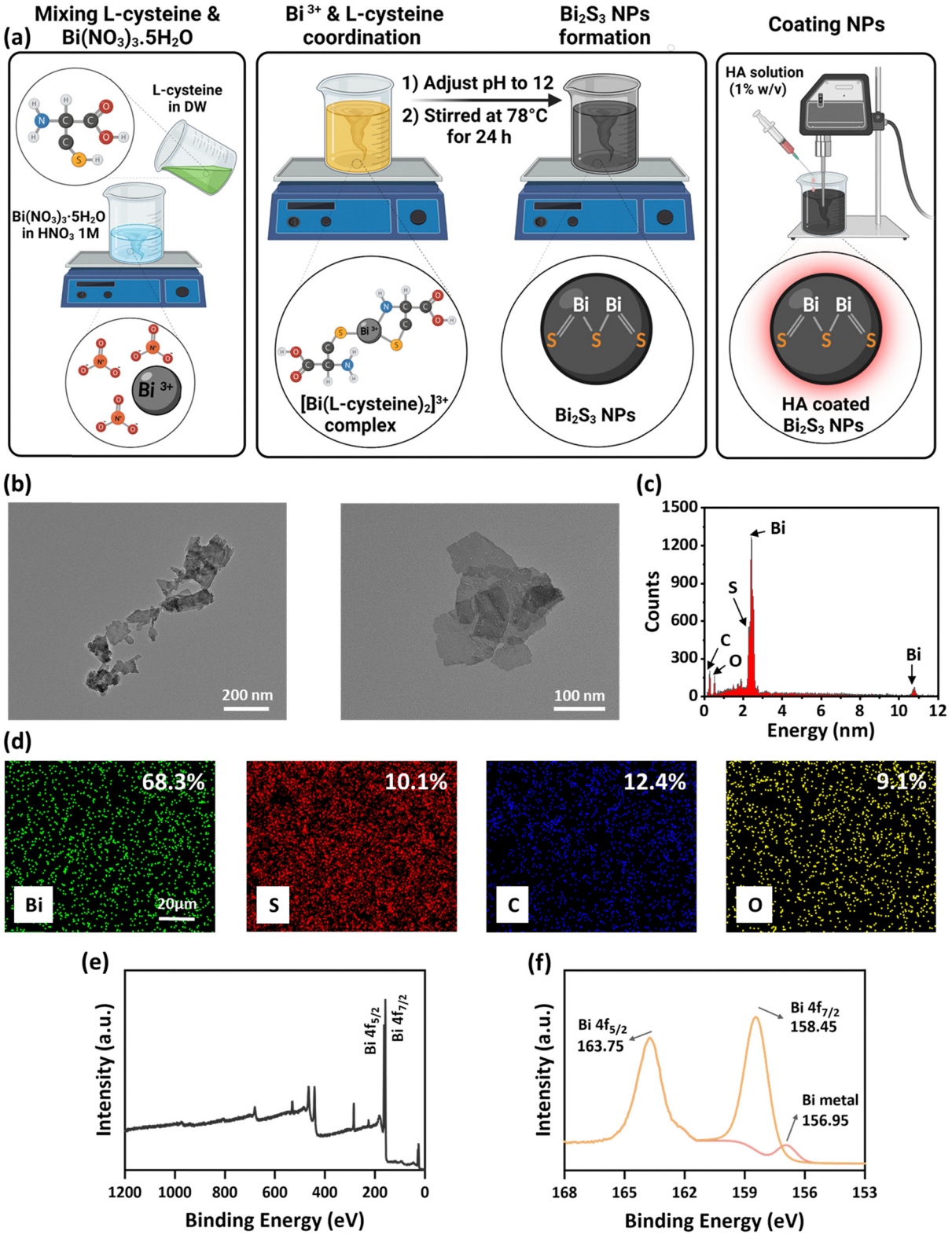

Fig. 2 (a) Schematic illustration of the synthesis process of BiH NPs. (b) TEM images of BiH NPs. (c) and (d) EDAX spectrum and elemental mapping of BiH NPs. (e) Wide-scan XPS spectrum of BiH NPs. (f) High-resolution Bi 4f spectra of BiH NPs.

percentage of degradation due to higher crosslinking density compared to other hydrogel samples, confirming the results obtained from gel content and water retention studies.

Therefore, G to A ration of 4.5 : 1 was chosen for Al loading and also preparing GA, GA–BiH, GA–Al, and GA–Al–BiH for the other following studies.

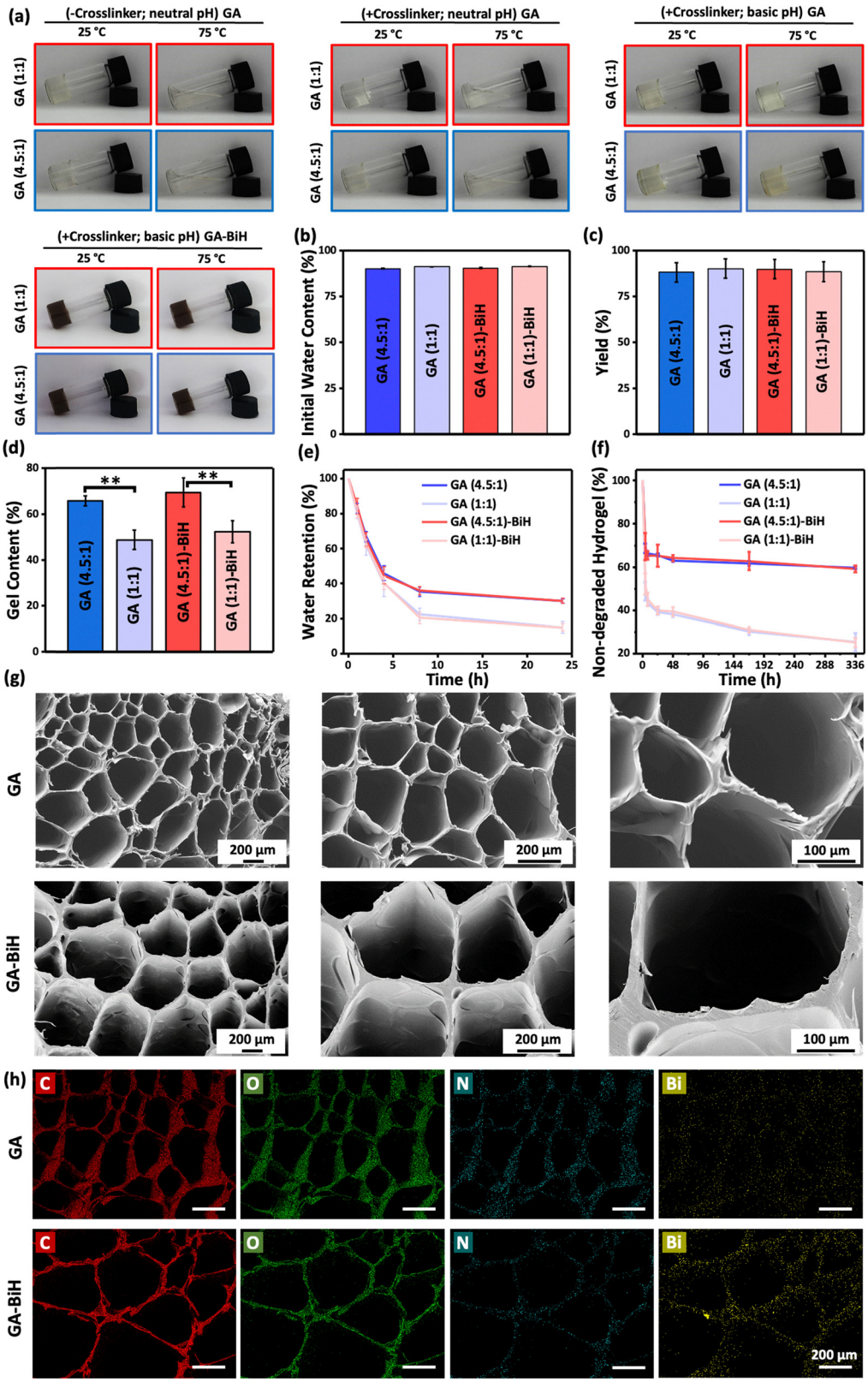

Fig. 3 (a) Photographs of GA mixture, GA, and GA–BiH hydrogel with two ratios of gelatin and sodium alginate (4.5 : 1 and 1 : 1) in neutral and basic conditions at room temperature and 75 °C. (b) IWC (%), (c) yield (%), (d) gel content (%), (e) water retention (%), and (f) non-degraded hydrogel percentage of GA(1 : 1), GA(1 : 1)–BiH, GA(4.5 : 1), and GA(4.5 : 1)–BiH hydrogels. All experiments were performed in triplicate, and data are reported as mean ± SD (N = 3). The statistical analysis was performed using one-way ANOVA (**$p < 0.01$). (g) SEM images and (h) elemental analysis of GA and GA–BiH hydrogels.

2.3.3. Morphological properties and elemental analysis of the hydrogels. The surface morphology of the GA and GA–BiH hydrogels was studied by scanning electron microscopy (SEM), revealing an interconnected porous microstructure (Fig. 3g). This porous structure aids wound closure by O_2 and exudate exchange, cell infiltration, growth, and sustained drug delivery.[27] Moreover, elemental analysis of GA–BiH hydrogel compared to the GA hydrogel represented a homogenous distribution of the Bi element within the walls of the hydrogel pores, indicating the uniform presence of the BiH NPs throughout the hydrogel matrix (Fig. 3h).

2.3.4. TGA and DTG studies. The thermal properties of initial ingredients and their conjugates were studied by thermogravimetric analysis (TGA) and derivative thermogravimetry (DTG), as shown in Fig. 4a. The maximum decomposition temperature and residual amount at 800 °C were summarized in Fig. 4b. All samples except Al and BiH NPs showed obvious weight loss at temperatures below 200 °C, indicating water loss and any evaporative components that adhere to the surface of hydrogels and their ingredients with weak bonds.[28] The second and main degradation step of sodium alginate from 206 °C to 283 °C corresponds to the degradation of saccharide structure, and the third weight loss step above 445 °C belongs to the formation of carbonaceous materials.[29] Moreover, the second and main weight loss of gelatin started at 251 °C owing to protein structure

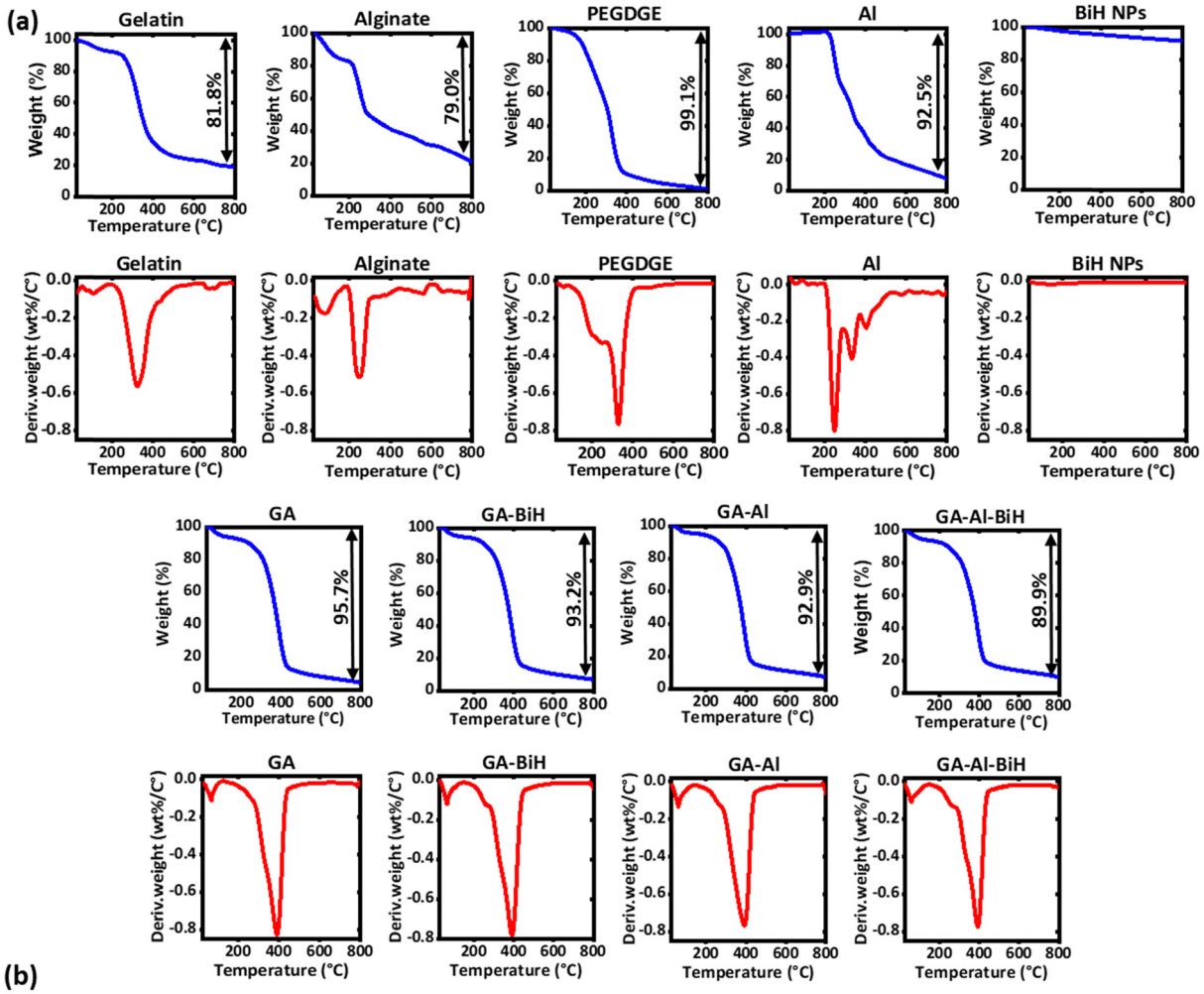

(b)

Type	Gelatin	Alginate	PEGDGE	Al	BiH	GA	GA-BiH	GA-Al	GA-Al-BiH
T_{Max} (°C)	322	247	329	248	----	389	390	391	392
Residue at 800 °C	19.2%	21.0%	0.9%	7.5%	91.4%	4.3%	6.8%	7.1%	10.1%

T_{max}: Maximum weight loss temperature

Fig. 4 (a) TGA and DTG profiles of the different hydrogels and their initial components. (b) The maximum destruction temperature and the residual weight at 800 °C of different hydrogels and initial components obtained from DTG and TGA, respectively.

degradation, and the third step was initiated at 642 °C due to the decomposition of intermediate products that are more heat stable.[30] The Al thermograph demonstrated three stages of decomposition at 200–500 °C that overlapped with each other in which the third stage related to the boiling point of Al.[31] The TGA curve of PEGDGE showed ongoing weight loss, and the main weight loss stage was in the range of 267 °C to 413 °C.[32] Also, synthesized BiH NPs represented high heat resistance even up to 800 °C. Furthermore, thermographic diagrams of all crosslinked hydrogels showed two stages of weight loss, and the second and main stages related to the destruction of the hydrogel structure. Based on Fig. 4b, the maximum decomposition temperature of GA, GA–BiH, GA–Al, and GA–Al–BiH hydrogels was at 389 °C, 390 °C, 391 °C, and 392 °C, respectively, which was higher in comparison to the initial ingredients, indicating that the crosslinking between free materials improved thermal stability. Moreover, Al and BiH NPs encapsulation in the hydrogel matrix had a slight positive effect on the maximum decomposition temperature. In addition, the residual weights of GA, GA–BiH, GA–Al, and GA–Al–BiH hydrogels at 800 °C were 4.3%, 6.8%, 7.1%, and 10.1%, respectively, indicating that the incorporation of Al and BiH NPs in the hydrogel matrix improved the thermal stability of the hydrogels. Also, the simultaneous addition of Al and BiH NPs had an additive effect on thermal stability.

2.3.5. XRD and ATR-FTIR. The X-ray diffraction (XRD) analysis was conducted to investigate the crystallinity of the gelatin, sodium alginate, Al, BiH NPs, GA, GA–BiH, GA–Al, and GA–Al–BiH samples (Fig. 5a). The diffractogram of sodium alginate consisted of two broad peaks at 13.9° and 21.9°, and gelatin showed a wide peak at 21.8° that is related to the collagen triple helical structure,[33] demonstrating the amorphous nature of both materials.[34] The XRD pattern of GA hydrogel showed only one broad peak at 21.7°, and diffraction peaks of sodium alginate disappeared at 13.7° and amplified at 21.9°, suggesting the intermolecular interaction between sodium alginate and gelatin influences the sodium alginate's structure.[35] The diffraction patterns of BiH NPs correspond to the standard pattern (JCPDS no. 170320).[36] The Diffractogram of Al displayed multiple sharp peaks, confirming the crystalline nature of Al.[26] Moreover, XRD patterns of GA–Al and GA–BiH hydrogels demonstrated that the intensity of the diffraction peak at 21.9° decreased, indicating that the addition of NPs and Al affected the placement order of GA hydrogel molecules. Furthermore, in GA–Al–BiH, the intensity of the diffraction peak at 21.9° extremely decreased, and there were multiple sharp peaks in 12°–22°, confirming the existence of BiH NPs and Al molecules, which together changed the arrangement of hydrogel molecules more than before to form crystalline microaggregates, and subsequently, leading to an increment of crystallinity.[34]

Attenuated total reflectance-Fourier transform infrared (ATR-FTIR) was conducted to evaluate the structure of the raw materials and crosslinked hydrogels in the range of 4000–400 cm^{-1} (Fig. 5b). The spectrum of gelatin showed a broad band at 3437 cm^{-1}, which is attributed to the –NH stretching vibration and –OH stretching vibration groups. The bands at 1655 cm^{-1} and 1533 cm^{-1} were assigned to the C=O stretching vibration of amide I (amide carbonyl) and –NH vibration of amide II, respectively.[37] Moreover, in the spectrum of sodium alginate, broad index peaks at 3440 cm^{-1}, 1576 cm^{-1}, and 1418 cm^{-1} were related to the OH stretching, –COO asymmetric, and symmetric stretching vibrations, respectively.[38] In the spectrum of PEGDGE, the absorption peaks at around 2867 cm^{-1} and 1096 cm^{-1} belong to the C–H stretching vibration and C–O stretching vibration, respectively. Absorption peaks at 844 cm^{-1} and 911 cm^{-1} were also attributed to the vibration of the epoxy ring.[39] The ATR-FTIR spectrum of GA, GA–BiH, GA–Al, and GA–Al–BiH hydrogels confirmed the presence of PEGDGE in the structure of the hydrogels by representing obvious peaks at around 2863 cm^{-1} and 1090 cm^{-1}, which belong to C–H stretching vibration bond and C–O stretching bond, respectively. In addition, weak absorption peaks at 911 cm^{-1} and 844 cm^{-1} in the ATR-FTIR spectrum of all hydrogels indicated the epoxy ring opening and formation of crosslinking.[40] Moreover, ATR-FTIR spectra of BiH NPs confirmed the formation of NPs by representing a sharp peak at 1382 cm^{-1} and a broad peak at 480 cm^{-1}, which corresponded to Bi–S bond vibration.[41,42] The remaining peak at 480 cm^{-1} in the spectra of GA–BiH and GA–Al–BiH hydrogels indicated successful nanoparticle loading in the hydrogel matrix. Furthermore, absorption peaks in the spectrum of Al appeared at 3434 cm^{-1} and 3340 cm^{-1} owing to the $-NH_2$ and –NH symmetric vibrations. In addition, the absorption peak at around 1704 cm^{-1} and 1780 cm^{-1} belong to the –C=O vibrations of the amid and ring of Al.[43] FTIR spectra of GA–Al and GA–Al–BiH demonstrated a shifted absorption peak at 1704 cm^{-1} to a higher wavelength after the insertion of Al, which indicates the establishment of hydrogen bonding between Al and hydrogel components.[44]

2.3.6. Rheological and mechanical properties. Rheological studies were conducted to evaluate the viscoelastic behavior of the GA–Al–BiH hydrogel. The strain sweep test exhibited the intersection of the G' and G'' values at around 350% at a constant frequency of 10 rad s^{-1} (Fig. S1), showing high tolerance to deformation before network breakage. Then, the frequency sweep showed higher values of G' compared to the G'', suggesting the semi-solid or hydrogel behavior of our biomaterial (Fig. S2). However, the GA mixture without using the crosslinker showed higher G'' values compared to the G', indicating the liquid nature of the sample (Fig. S3).

Compressive stress–strain measurement was studied to evaluate the mechanical strength of the GA mixture, GA, GA–BiH, GA–Al, and GA–Al–BiH hydrogels (Fig. 5c). The GA mixture did not tolerate 50% of compressive strain and tore up, while all crosslinked hydrogels retained the original shape after pressure, confirming the formation of strong bonds in crosslinked hydrogels. The maximum compressive stress was reported as 30.4 ± 3.0 kPa, 529.8 ± 10.8 kPa, 567.1 ± 11.4 kPa, 544.5 ± 8.9 kPa, 587.1 ± 15.2 kPa for GA mixture, GA, GA–BiH, GA–Al, and GA–Al–BiH hydrogels, respectively (Fig. 5d and e). The remarkably high values of compressive stress of crosslinked hydrogels in comparison to the GA mixture proved the increased mechanical tolerance resulted from the addition of PEGDGE to the GA

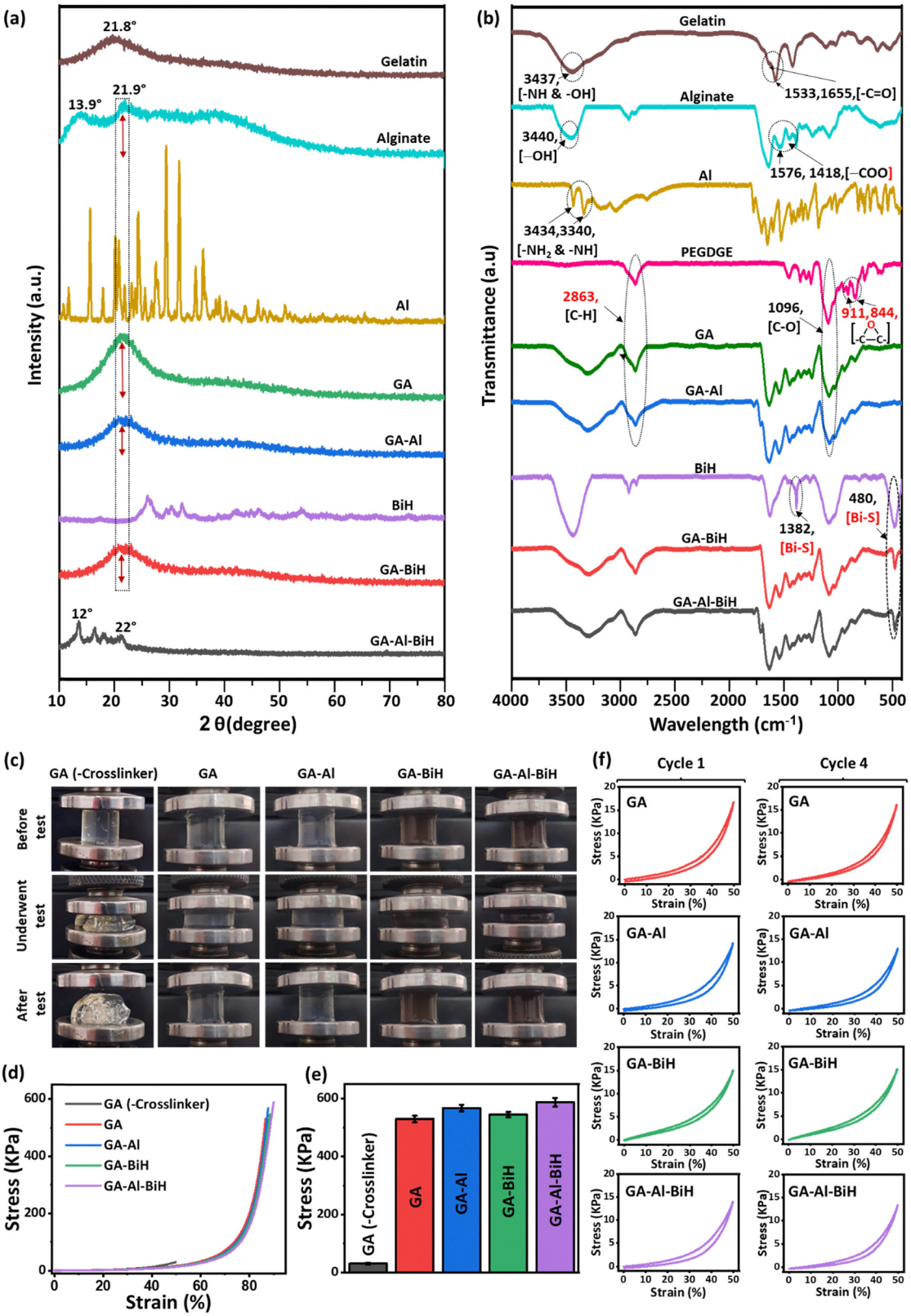

Fig. 5 (a) XRD patterns and (b) ATR-FTIR spectra of the pure ingredients and prepared hydrogels. (c) Photographs of GA (-crosslinker) mixture and crosslinked hydrogels (GA, GA–BiH, GA–Al, and GA–Al–BiH) before, underwent, and after compressive test at 50% strain. (d) Compressive stress–strain curve and (e) maximum compressive deformation point of GA (-crosslinker) mixture and crosslinked hydrogels. (f) Compressive stress–strain curve of crosslinked hydrogels at 50% compressive strain after one and four loading–unloading cycles.

mixture. Noticeably, embedding Al and BiH NPs within the GA hydrogel slightly increased the mechanical strength, indicating the formation of new interactions like hydrogen bonding between these materials and hydrogel components. It has previously been shown that the insertion of Al into the gelatin–chitosan scaffold structure up to 0.5% (w/v) increases the mechanical resistance.[45] Compressive stress–strain curves after multiple loading–unloading cycles demonstrated an obvious hysteresis loop in GA, GA–BiH, GA–Al, and GA–Al–BiH hydrogels, retaining their original curved shapes without any rupture in different cycles (Fig. 5f). Therefore, good flexibility and excellent mechanical properties of these hydrogels can simulate skin elasticity to facilitate air infiltration into the wound and protect it from peripheral damage to heal faster.[46]

2.4. Photothermal behavior of BiH NPs and hydrogels

The *in vitro* photothermal studies were performed to evaluate the light-to-heat conversion capacity of NPs to reach the maximum bactericidal and wound regeneration effect with the lowest risk of damage to healthy tissues in m-PTT. BiH NPs displayed concentration-dependent temperature change under 808 nm NIR irradiation with the power density of 1 W cm^{-2} for 10 min, rising to 41.2 °C, 46 °C, and 52 °C with 50 μg ml^{-1}, 100 μg ml^{-1}, and 200 μg ml^{-1} concentrations of the NPs solution, respectively (Fig. 6a). Generally, temperatures above 50 °C were used to kill bacteria;[47] however, the risk of damage to healthy tissues is considered an alarming challenge. Since the appropriate temperature for m-PTT is around 42 °C, 100 μg ml^{-1} of BiH NPs can be an excellent choice for incorporation inside the hydrogels by controlling the temperature by

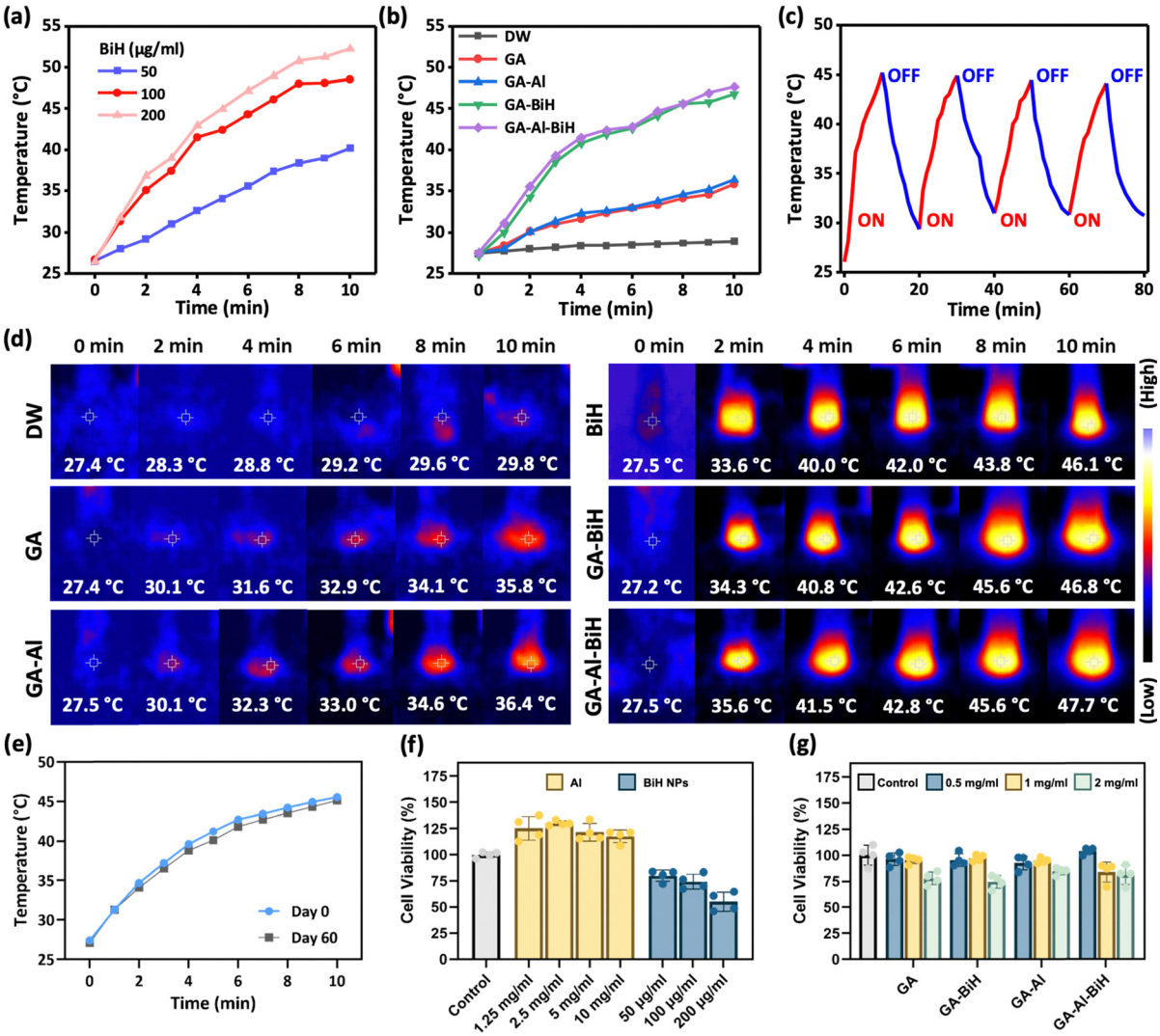

Fig. 6 Photothermal temperature curves of (a) different concentrations of BiH NPs, (b) DW, GA, GA–Al, GA–BiH, and GA–Al–BiH hydrogels under 808 nm NIR laser irradiation (1 W cm^{-2}) for 10 min. (c) Temperature curves of GA–Al–BiH hydrogel during four ON/OFF cycles of laser irradiation (808 nm laser, 1 W cm^{-2}). (d) Infrared images of various samples upon 808 nm NIR laser irradiation (1 W cm^{-2}) for 10 min. (e) Temperature curves of the 100 μg ml^{-1} BiH NPs on two different days under 808 nm NIR laser irradiation (1 W cm^{-2}) for 10 min. Viabilities of HDFa cells after exposure to different concentrations of the (f) Al, BiH NPs, (g) GA, GA–BiH, GA–Al, and GA–Al–BiH hydrogels incubated for 24 h at 37 °C, quantified by the CellTiter-Glo luminescence assay. Data are presented as the mean ± SD (N = 4).

reducing the irradiation time or increasing the distance between the laser and the sample.[48] Moreover, the photothermal behavior of GA and GA–Al hydrogels under 808 nm NIR radiation (1 W cm^{-2}, 10 min) did not demonstrate significant temperature changes compared to distilled water (DW) as a control group (Fig. 6b). However, the temperature of the GA–BiH and GA–Al–BiH hydrogels significantly increased up to 46.8 °C and 47.7 °C, respectively. Furthermore, GA–Al–BiH hydrogel after four cycles of heating and cooling phases by NIR laser confirmed the suitable photothermal stability, suggesting the outstanding potential of this photoactive agent for multiple PTT usage with a single injection of the hydrogel (Fig. 6c). The infrared images were consistent with the data represented in Fig. 6b, suggesting the satisfactory photothermal effect of the BiH, both alone or when incorporated into the hydrogel system (Fig. 6d). Moreover, BiH NPs exhibited excellent stability, maintaining consistent photothermal performance even after two months of being stored at 4 °C (Fig. 6e).

2.5. Cell viability assay

The cytotoxicity of the hydrogels and hydrogel ingredients with different concentrations were assessed on primary dermal fibroblasts (HDFa) after 24 h of incubation time to ensure the intrinsic biocompatibility. All in all, concentrations up to 10 mg ml^{-1} (equivalent to our formulation) demonstrated favorable cytocompatibility. BiH NPs with concentrations of 50 μg ml^{-1}, 100 μg ml^{-1}, and 200 μg ml^{-1} exhibited 80%, 75%, and 55% of cell viability, respectively. Thus, together with PTT results 100 μg ml^{-1} concentration of the BiH NPs was selected to embed inside the hydrogels to show efficient PTT effect without cytotoxic effect on healthy cells surrounding the wound area. Moreover, GA, GA–BiH, GA–Al, and GA–Al–BiH hydrogels with different concentrations up to 2 mg ml^{-1} exhibited desirable cytocompatibility, making them a promising candidate for biomedical applications, such as wound healing.

2.6. *In vitro* antibacterial activity

Bacterial infection by prolongation of the inflammatory response may lead to increased levels of matrix metalloproteases, which could damage the ECM and delay the wound healing process by facilitating the wound to enter the chronic phase.[49] PTT could eliminate the bacteria in three steps: (1) adsorption and interaction of photothermal agents on the surface of bacteria; (2) conversion of light into heat and increment of the surface temperature of bacteria; and (3) denaturation of enzymes.[50] Although there are some concerns about damage to healthy surrounding tissues by PTT, m-PTT with mild temperature rise is considered a more suitable strategy for bacterial elimination. The antibacterial ability of BiH (100 μg ml^{-1}), Al (1% w/v), GA, GA–BiH, and GA–Al–BiH hydrogels was investigated against Gram-negative *E. coli* and Gram-positive *S. aureus* with and without laser irradiation using the colony counting method (Fig. 7a and b). The growth of *E. coli* colonies was eradicated more than *S. aureus* in GA–BiH, and GA–Al–BiH treated groups with or without NIR radiation. The peptidoglycan multilayer cell wall of Gram-positive bacteria makes them more resistant compared to Gram-negative bacteria, with a thin cell wall.[10] GA–BiH hydrogel exhibited 90.0% and 59.3% of *E. coli* and *S. aureus* colony elimination, respectively, owing to the laser-induced temperature increment effect.

These values increased to 98% and 89.8% of *E. coli* and *S. aureus* colony destruction with GA–Al–BiH hydrogel. While the Al solution did not show any direct antibacterial effect, the incorporation of Al inside our hydrogel formulation enhanced the antibacterial efficacy in both bacteria in an additive or synergistic way, possibly by enhancing the susceptibility of bacterial membranes to PTT-induced hyperthermia. However, control, BiH, GA, and GA–Al hydrogel groups, even upon 808 nm NIR radiation, showed normal bacterial growth. Although the BiH NPs + laser irradiation group was able to increase the temperature up to 45–46 °C, the antibacterial effect was unsatisfactory due to rapid heat dissipation and aggregation of NPs in solution compared to solid or semi-solid matrices such as a hydrogel. Hence, *in vitro* antibacterial evaluations showed that the m-PTT, alongside the presence of Al inside the hydrogel, is a powerful tool in a hydrogel to eliminate bacterial infections.

2.7. *In vitro* hemocompatibility assay

Hemocompatibility is one of the elementary and vital requirements of any dressing material, which can be investigated through a hemolysis test.[51] *In vitro* hemocompatibility of GA, GA–Al, GA–BiH, and GA–Al–BiH hydrogels was carried out in different concentrations (1 mg ml^{-1}, 2 mg ml^{-1}, and 3 mg ml^{-1}) and different time points (2 h, 4 h, 8 h, and 24 h). The negative control group and hydrogel-treated samples in different concentrations and time points demonstrated a transparent supernatant with a slight red color at the bottom of the tubes, demonstrating packed non-hemolyzed RBCs (Fig. 7c). However, RBCs treated with DW as a positive control showed a bright red supernatant, indicating the rupture of RBC and release of the hemoglobin into the medium. Moreover, as shown in Fig. 7d, all hydrogels in different concentrations and time points are considered non-hemolytic biomaterials (non-hemolyzed RBCs $>98\%$) based on the critical safe margin according to ISO/TR 7406 ($<5\%$ hemolysis ratio for biomaterials).[52] Also, the presence of the BiH NPs (100 μg ml^{-1}) in GA–BiH and GA–Al–BiH hydrogels did not have a negative effect on the hemolysis ratio.

2.8. *In vivo* toxicity

To evaluate the biological safety and biocompatibility of the GA, GA–BiH, GA–Al, and GA–Al–BiH hydrogels, hematological and biochemical factors of blood were measured. All hematological index in the Tegaderm™, GA, GA–BiH, GA–Al, and GA–Al–BiH treated groups, including blood levels of RBCs, hemoglobin (HGB), hematocrit (HCT), platelet (PLT), white blood cells (WBCs), neutrophils (NEUT), lymphocytes (LYMPH), and monocytes (MONO) had no significant difference compared to the control group. Furthermore, the biochemical factors and minerals, such as total protein (TP), calcium (Ca), phosphorus (Ph), blood urea nitrogen (BUN), creatinine (CERA), lactate dehydrogenase (LDH), and alkaline phosphatase (ALP) showed no obvious

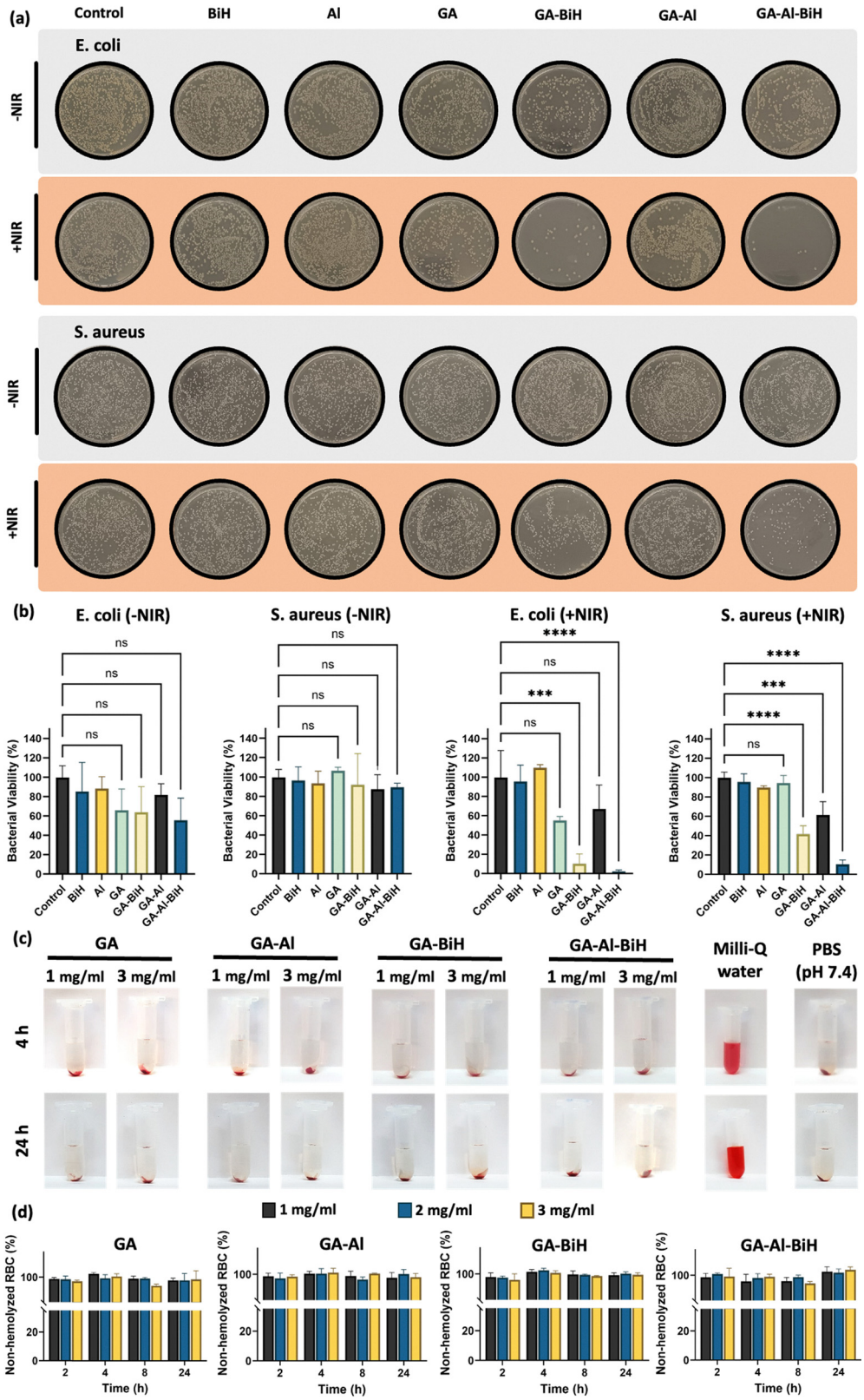

Fig. 7 (a) Representative images of bacterial growth and (b) bacterial viability graphs of *E. coli* and *S. aureus* suspensions on agar plates treated with PBS (as a control), BiH (100 μg ml^{-1}), Al (1% w/v), GA, GA–BiH, and GA–Al–BiH hydrogels with and without NIR irradiation after 24 h of incubation (1 W cm^{-2}, 10 min). Data are reported as the mean ± SD (N = 3). The statistical analysis was performed using one-way ANOVA (***$p < 0.001$, ****$p < 0.0001$, and ns = not significant *vs.* control group). (c) Photographs of different samples with concentrations of 1 mg ml^{-1} and 3 mg ml^{-1} exposed to the human RBCs after 4 h and 24 h incubation. (d) The non-hemolyzed RBCs (%) after treatment with various hydrogels with different concentrations after different time points of co-incubation.

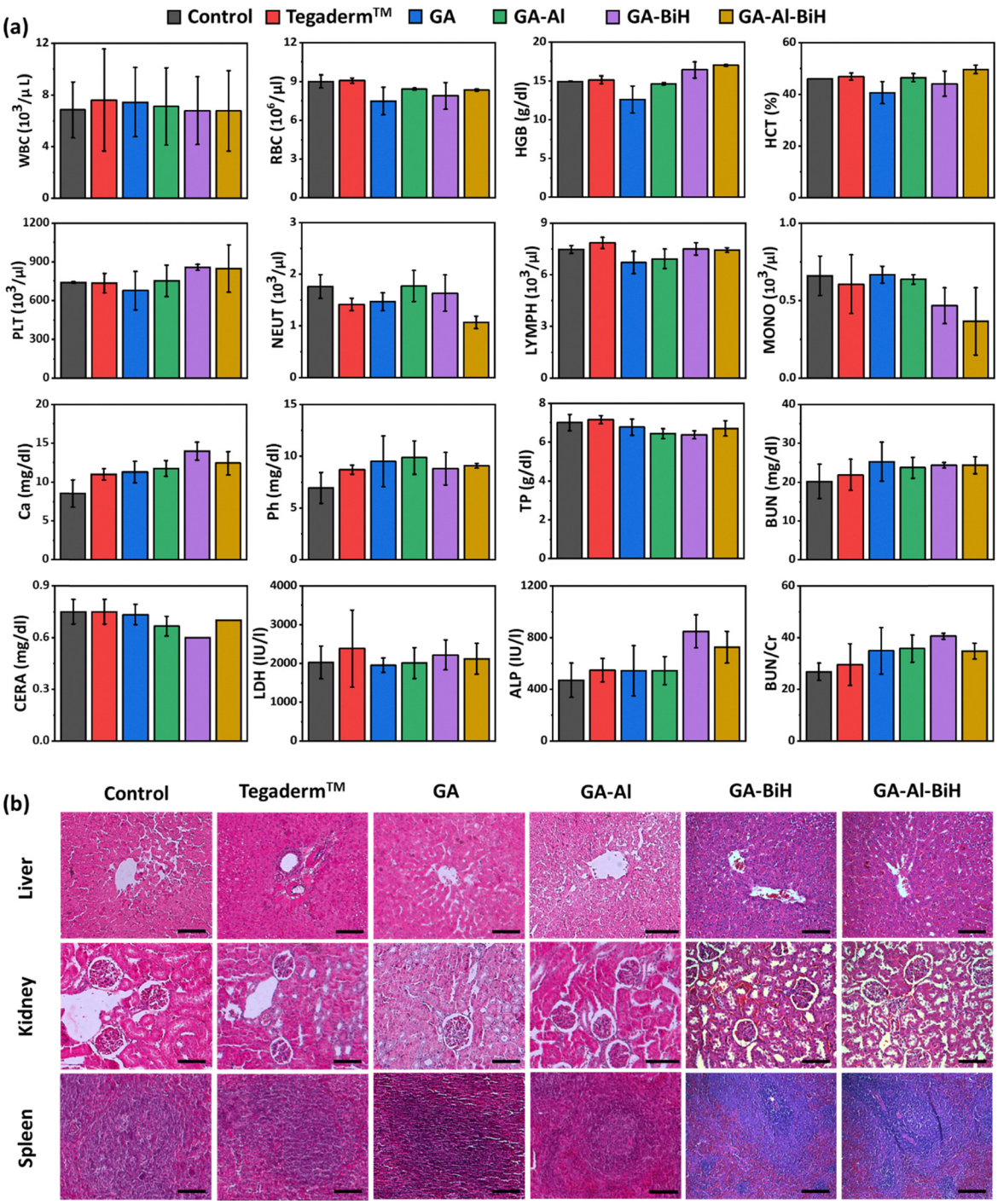

Fig. 8 *In vivo* toxicity evaluation of GA, GA–BiH, GA–Al, and GA–Al–BiH hydrogels in full-thickness rat skin incision model. (a) Biochemical and hematological indexes of animals for control, Tegaderm™, GA, GA–BiH, GA–Al, and GA–Al–BiH hydrogels. Data are reported as the mean ± SD (N = 5). (b) The H&E-stained tissues of the kidney, liver, and spleen of rats 14 days after subcutaneous injection of different samples. Scale bar = 0.1 mm.

toxicity in the treated groups (Fig. 8a). Additionally, hematoxylin & eosin (H&E) staining was used for histological analysis of the important organs of rats, including the kidney, liver, and spleen, after 14 days of subcutaneous injection of different hydrogels. No apparent histopathological changes, such as tissue death, changes in cell structure, and even the symptoms of inflammation, were seen, confirming the low systemic toxicity and good biocompatibility of the GA, GA–BiH, GA–Al, and GA–Al–BiH hydrogels (Fig. 8b).

2.9. *In vivo* wound healing

The advantages of accelerated wound healing rely on less inflammation, infection, and scar formation by minimizing the time of exposed wound.[53] Accordingly, the wound healing

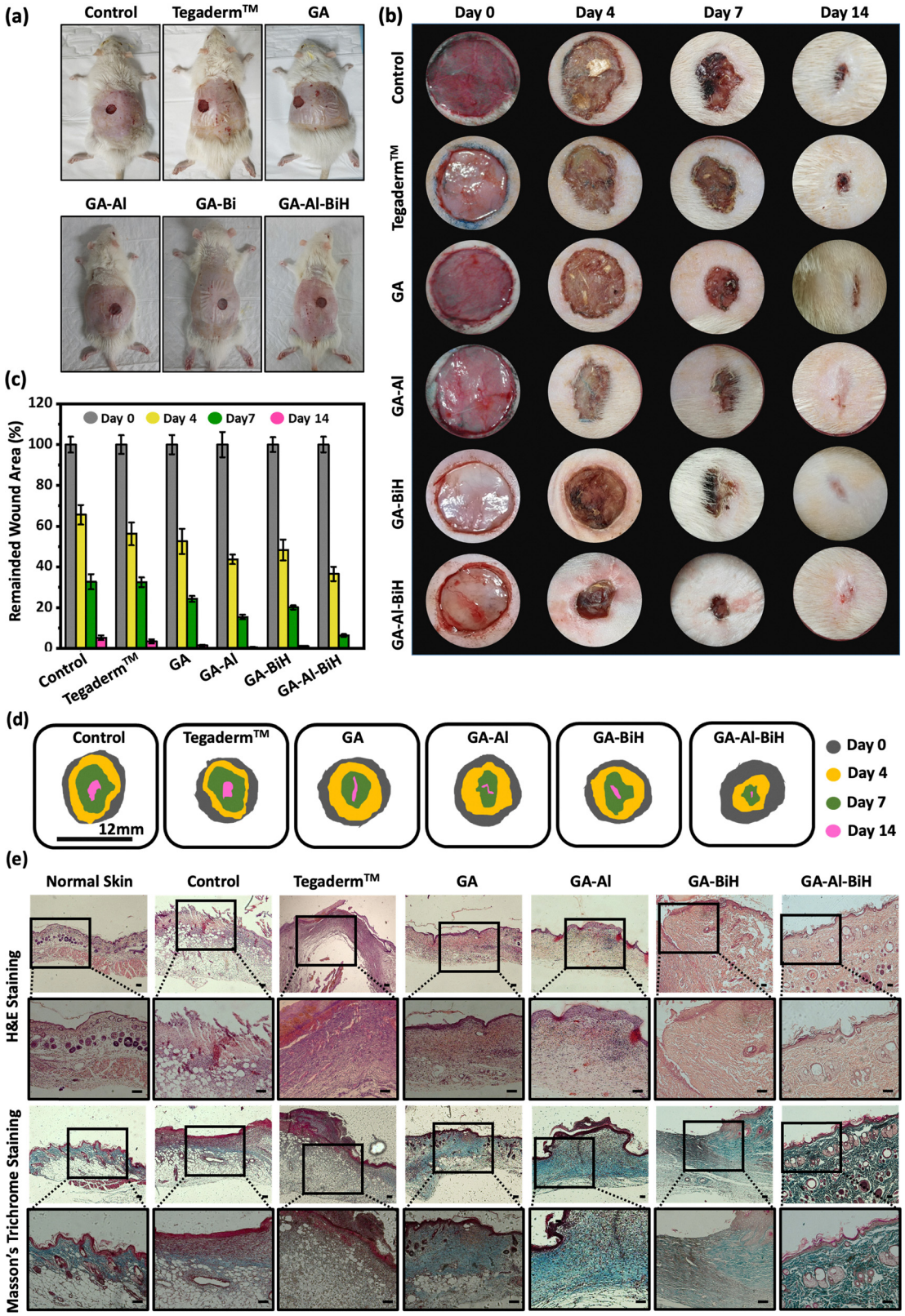

Fig. 9 *In vivo* wound healing assessment. (a) Photographs of full-thickness incisions created on the back of the rat in control, Tegaderm™, GA, GA–BiH, GA–Al, GA–Al–BiH hydrogel-treated groups on the first day of the treatment. (b) Skin photographs of wound healing in a full-thickness wound model in control, Tegaderm™, GA, GA–BiH, GA–Al, and GA–Al–BiH hydrogels on days 0, 4, 7, and 14 after treatment. Photographs were taken from a representative animal of each group. (c) Remained wound area (%) in different treated groups on days 0, 4, 7, and 14 after treatment. Data are reported as the mean ± SD (N = 5). The statistical analysis was performed using one-way ANOVA (**$p < 0.01$, ***$p < 0.001$ *vs.* the control group). (d) Schematic traces of wound healing of one animal in each group during 14 days for different treatments (scale bar = 12 mm). (e) H&E and Masson's trichrome-stained wound tissues in different groups after 14 days of treatment with different magnifications. Scale bar = 100 μm.

capacity of GA, GA–BiH, GA–Al, and GA–Al–BiH hydrogels was investigated by a circular full-thickness wound model on the dorsal area of rats (Fig. 9a). To evaluate the wound healing process, the wound site of various treated groups was photographed on days 0, 4, 7, and 14 after surgery, and a schematic diagram of each wound area was depicted (Fig. 9b). In this study, Tegaderm™, a widely accepted transparent wound dressing, was used as a control positive group that protects the wound from external contaminants, while providing moisture vapor and gas exchange.[54] GA–Al–BiH hydrogel-treated group showed the smallest remaining wound across all time points compared to the other groups, offering rapid wound closure (Fig. 9c and d). GA–BiH and GA–Al treated groups represented smaller wound areas compared to the GA treated group, indicating the positive effect of Al and BiH NPs on wound healing. Moreover, H&E-stained wound samples of GA, GA–BiH, GA–Al, and GA–Al–BiH groups demonstrated fewer inflammatory cells compared to the control group and Tegaderm™-treated groups after 14 days of treatment (Fig. 9e). The GA–Al–BiH-treated group did not show any obvious population of inflammatory cells, resulting in faster wound re-epithelialization. In addition, the development of skin appendages such as hair follicles and sebaceous glands, as well as numerous blood vessels in the GA–Al–BiH-treated group, proposed the complete regeneration of the damaged skin tissue. In fact, we expected these results owing to the cell proliferation acceleration properties of Al, the antibacterial effect of the BiH NPs, and the ECM mimicking effect of the hydrogel. In addition, the blue-green color in Masson's trichrome-stained samples represented the deposition of collagen, which is synthesized during the remodeling and proliferative phases of wound regeneration.[53] Collagen was mostly observed in the GA–Al–BiH-treated group, indicating the improvement of the wound healing procedure. In summary, the results of the remained wound

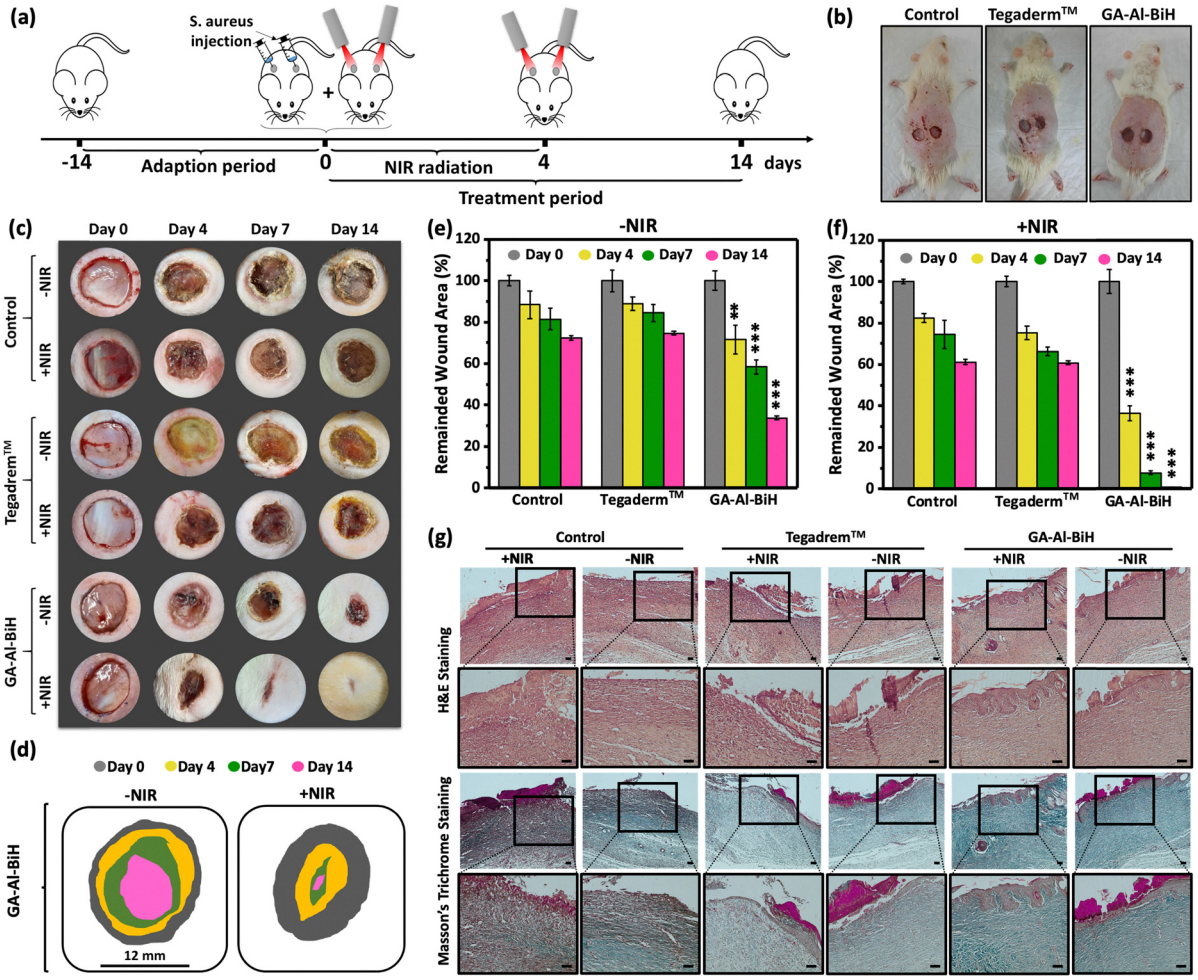

Fig. 10 Infected-wound healing assessment. (a) Schematic procedure of creating an infectious wound and the treatment procedure upon 14-day study. (b) Photographs of two full-thickness incisions created on the back of the rat in control, Tegaderm™, and GA–Al–BiH hydrogel treated groups on the first day of the experiment. (c) Skin photographs of wound healing in full-thickness wound model in control, Tegaderm™, and GA–Al–BiH hydrogel treated groups with and without NIR irradiation (10 min, 1 W cm^{-2}) on days 0, 4, 7, and 14 after treatment. Photographs were taken from a representative animal of each group. Scale bar: 12 mm. (d) Schematic traces of wound healing of GA–Al–BiH treated group during 14 days with and without NIR irradiation. (e) and (f) Remained wound area (%) in different treated groups on days 0, 4, 7, and 14 of treatment with and without NIR irradiation (10 min, 1 W cm^{-2}). Data are shown as mean ± SD (N = 5). The data were statistically analysed using one-way ANOVA (**$p < 0.01$, ***$p < 0.001$). (g) H&E and Masson's trichrome-stained infected wound tissues in different groups with and without NIR irradiation (10 min, 1 W cm^{-2}) after 14 days. Scale bar 100 μm.

area, H&E staining, and Masson's trichrome staining manifested that GA–Al–BiH hydrogel has the potential to accelerate wound tissue renewal.

2.10. *In vivo* infected wound assessment

Infection is one of the factors that could delay the wound healing process by prolonging the inflammatory phase.[55] The wound closure capacity and antibacterial activity of GA–Al–BiH hydrogel with and without NIR irradiation (808 nm, 1 W cm^{-2}, 3 min) were evaluated by the creation of two *S. aureus*-infected full-thickness wounds on the dorsal region of the rats (Fig. 10a and b). On the 4th day post-surgery, clear yellow pus or pathogen contamination appeared in the control and Tegaderm™ groups, either with or without NIR irradiation, and remained during the following days over the 14-day study, resulting in a reduction in the wound closure rate (Fig. 10c). Mild heat generation, besides the antibacterial activities of GA–Al–BiH, resulted in no obvious infection and a satisfactory wound healing rate in the animals treated with this group (99.3 ± 0.2%) (Fig. 10d). However, the remaining wound area for control ± NIR and Tegaderm™ ± NIR was above 60%, due to the uncontrolled infection (Fig. 10e and f). Compared to the previously reported hydrogel-based mPTT platforms, our formulation outperformed them in accelerated wound closure. For instance, 22% of the remaining wound area was observed after 7 days of treatment with a carboxymethyl chitosan/polyethylene glycol/graphene oxide hydrogel with multiple NIR irradiations with a power density of 2 W cm^{-2} for 5 min.[56] In another work, carboxymethyl chitosan/polyvinyl alcohol/oxidized hyaluronic acid/dopamine hydrogel exhibited around 30% of the remained wound area on day 7 of treatment using NIR irradiation (1.0 W cm^{-2}) for 5 min on days 1 to 5.[57] However, on the same day of treatment around 8% of wound area remained with our system utilizing a lower power density of NIR (1 W cm^{-2}) and less irradiation time (2 min).

Additionally, H&E-stained wound tissues did not represent an organized epidermal structure in the control, control + NIR, Tegaderm™, and Tegaderm™ + NIR groups, which indicated the inflammatory phase (Fig. 10g). In the GA–Al–BiH and GA–Al–BiH + NIR-treated groups, the regeneration of the epithelium progressed, and a smaller amount of inflammatory cell infiltration was observed compared to other groups. In addition, the GA–Al–BiH + NIR-treated group displayed a high amount of skin appendages such as hair follicles and sebaceous glands, which confirmed the final stages of skin regeneration. Moreover, Masson's trichrome-stained wound samples showed GA–Al–BiH + NIR-treated group had the highest collagen deposition, which was deeper, thicker, and better arranged, resembling normal skin, compared to other groups. Collectively, these results confirmed that the designed GA–Al–BiH hydrogel is a good candidate for antibacterial wound dressing, owing to the antibacterial activity and the m-PTT effect.

3. Conclusion

In summary, a photoactive ECM-mimicking hydrogel with high mechanical strength, desirable biosafety, and excellent antibacterial activity is designed for m-PTT-induced tissue regeneration. A chemically crosslinked hydrogel matrix with high initial water content and low water retention rate is considered a suitable carrier for embedding Al and BiH NPs. *In vitro* antibacterial evaluation manifested m-PTT leading to ablation of *E. coli* and *S. aureus*. Moreover, hyperthermia triggered by m-PTT and regenerative properties of Al remarkably promoted wound regeneration by acceleration of re-epithelialization and collagen synthesis. According to this satisfactory behavior, multifunctional GA–Al–BiH hydrogel provides a strategy for infected wound repair.

Ethical standards

In all animal studies, the animals were housed in the animal room two weeks before every experiment to adapt to the new environment. Generally, animals were housed as one per cage at a 12 h light/dark cycle with an environmental temperature of 21–23 °C and relative humidity of 50–60%. The Committee of Animal Experimentation guidelines of "Zanjan University of Medical Sciences" approved all laboratory procedures in animal experiments with an ethical code of IR.ZUMS.REC.1399.102.

Conflicts of interest

There are no conflicts to declare.

Data availability

Supplementary information is available. See DOI: **https://doi.org/10.1039/d5tb01346a**

The data analysis of this article is available in the interactive notebook of Mostafa Qahremani and can be provided upon request from the authors.

Acknowledgements

This study was financially supported by the School of Pharmacy, Zanjan University of Medical Sciences, Zanjan, Iran, under the framework of the thesis project (No. A-12-1296-6) with the ethical code of IR.ZUMS.REC.1399.102. M.-A. Shahbazi and H. A. Santos acknowledge UMCG Research Funds for financial support.

References

1 Y. Zang, W. Zhang, P. Wang, C. Zhu, X. Guo, W. Wang, L. Cheng, X. Chen and X. Wang, *Adv. Healthcare Mater.*, 2025, **14**, 2401810.
2 H. Zhu, H. T. Ao, Y. Fu, C. Zou, Z. Chen, Z. Jin, H. Zhou, B. Sun and S. Guo, *Int. J. Biol. Macromol.*, 2024, **275**, 133524.
3 J. He, M. Shi, Y. Liang and B. Guo, *Chem. Eng. J.*, 2020, **394**, 124888.

4 Y. P. Jia, K. Shi, F. Yang, J. F. Liao, R. X. Han, L. P. Yuan, Y. Hao, M. Pan, Y. Xiao, Z. Y. Qian and X. W. Wei, *Adv. Funct. Mater.*, 2020, **30**, 2001059.
5 Y. Zhou, H. Feng, Y. Jiang, G. Hua, Q. Zhang, S. Zeng, W. Li, L. Li, N. Kang and L. Ren, *ACS Appl. Mater. Interfaces*, 2021, **13**, 18443–18453.
6 S. Zhou, X. Zhang, W. Ni, Y. He, M. Li, C. Wang, Y. Bai, H. Zhang and M. Yao, *Adv. Healthcare Mater.*, 2024, **13**, 2400003.
7 M. Patel and A. Prabhu, *Int. J. Pharm.*, 2022, **618**, 121697.
8 H. Feng, T. Wang, W. Wang, C. Ma, Y. Pu and S. Chen, *J. Mater. Sci. Technol.*, 2024, **173**, 121–136.
9 H. Guo, X. Zhao, H. Sun, H. Zhu and H. Sun, *Nanotechnology*, 2018, **30**, 75101.
10 D. Ayodhya and G. Veerabhadram, *Mater. Today Chem.*, 2020, **17**, 100320.
11 S. Tamilvanan, G. Gurumoorthy, S. Thirumaran and S. Ciattini, *Polyhedron*, 2017, **123**, 111–121.
12 S. Yan, S. Xu, Y. Wang, J. You, C. Guo and X. Wu, *Adv. Healthcare Mater.*, 2024, **13**, 2400884.
13 Y. Liu, Q. Ma, L. Tang, Y. Shen, H. Zhao, X. Liu, D. Lin and G. Zhou, *Chem. Eng. J.*, 2024, **497**, 154518.
14 E.-Y. Chuang, Y.-C. Lin, Y.-M. Huang, C.-H. Chen, Y.-Y. Yeh, L. Rethi, Y.-J. Chou, P.-R. Jheng, J.-M. Lai, C.-J. Chiang and C.-C. Wong, *Carbohydr. Polym.*, 2024, **339**, 122174.
15 A. S. Vaziri, E. Vasheghani-Farahani, S. Hosseinzadeh, F. Bagheri, M. Büchner, D. W. Schubert and A. R. Boccaccini, *Biomacromolecules*, 2024, **25**, 2323–2337.
16 V. Nosrati-Siahmazgi, S. Abbaszadeh, K. Musaie, M. R. Eskandari, S. Rezaei, B. Xiao, F. Ghorbani-Bidkorpeh and M.-A. Shahbazi, *Mater. Today Bio*, 2024, **26**, 101062.
17 N. Wang, K.-K. Yu, K. Li and X.-Q. Yu, *J. Mater. Chem. B*, 2023, **11**, 6934–6942.
18 Y. Feng, S. Qin, Y. Yang, H. Li, Y. Zheng, S. Shi, J. Xu, S. Wen and X. Zhou, *Colloids Surf., B*, 2024, **241**, 114058.
19 B. Özçelik, M. Kartal and I. Orhan, *Pharm. Biol.*, 2011, **49**, 396–402.
20 L. U. Araújo, A. Grabe-Guimarães, V. C. F. Mosqueira, C. M. Carneiro and N. M. Silva-Barcellos, *Acta Cir. Bras.*, 2010, **25**, 460–466.
21 B. Zhang, X. Ye, W. Hou, Y. Zhao and Y. Xie, *J. Phys. Chem. B*, 2006, **110**, 8978–8985.
22 E. Miniach and G. Gryglewicz, *J. Mater. Sci.*, 2018, **53**, 16511–16523.
23 S. Abbaszadeh, M. R. Eskandari, V. Nosrati-Siahmazgi, K. Musaie, S. Mehrabi, R. Tang, M. R. Jafari, B. Xiao, V. Hosseinpour Sarmadi, F. Haghi, B. Z. Chen, X. D. Guo, H. A. Santos and M.-A. Shahbazi, *Mater. Today Bio*, 2023, **19**, 100609.
24 G. Vargas, J. L. Acevedo, J. López and J. Romero, *Mater. Lett.*, 2008, **62**, 21–22.
25 A. Karimi and M. Navidbakhsh, *Biomed. Technol.*, 2014, **59**, 479–486.
26 Z. Ahmadian, A. Correia, M. Hasany, P. Figueiredo, F. Dobakhti, M. R. Eskandari, S. H. Hosseini, R. Abiri, S. Khorshid, J. Hirvonen, H. A. Santos and M. Shahbazi, *Adv. Healthcare Mater.*, 2021, **10**, 2001122.
27 P. Lu, D. Ruan, M. Huang, M. Tian, K. Zhu, Z. Gan and Z. Xiao, *Signal Transduction Targeted Ther.*, 2024, **9**, 166.
28 K. Dharmalingam and R. Anandalakshmi, *Int. J. Biol. Macromol.*, 2019, **134**, 815–829.
29 B. Sarker, D. G. Papageorgiou, R. Silva, T. Zehnder, F. Gul-E-Noor, M. Bertmer, J. Kaschta, K. Chrissafis, R. Detsch and A. R. Boccaccini, *J. Mater. Chem. B*, 2014, **2**, 1470–1482.
30 J. F. Martucci, A. Vázquez and R. A. Ruseckaite, *J. Therm. Anal. Calorim.*, 2007, **89**, 117–122.
31 G. Svetlichny, I. C. Külkamp-Guerreiro, D. F. Dalla Lana, M. D. Bianchin, A. R. Pohlmann, A. M. Fuentefria and S. S. Guterres, *J. Drug Delivery Sci. Technol.*, 2017, **40**, 59–65.
32 M. A. Gámiz González, U. Edlund, A. Vidaurre and J. L. Gómez Ribelles, *Polym. Int.*, 2017, **66**, 1624–1632.
33 C. Peña, K. de la Caba, A. Eceiza, R. Ruseckaite and I. Mondragon, *Bioresour. Technol.*, 2010, **101**, 6836–6842.
34 H. E. Thu and S. F. Ng, *Int. J. Pharm.*, 2013, **454**, 99–106.
35 D. Nkurunziza, T. C. Ho, R. A. Protzman, Y. J. Cho, A. T. Getachew, H. J. Lee and B. S. Chun, *J. Supercrit. Fluids*, 2021, **169**, 105120.
36 C. Lu, Z. Li, L. Yu, L. Zhang, Z. Xia, T. Jiang, W. Yin, S. Dou, Z. Liu and J. Sun, *Nano Res.*, 2018, **11**, 4614–4626.
37 S. R. Derkach, N. G. Voron'ko, N. I. Sokolan, D. S. Kolotova and Y. A. Kuchina, *J. Dispersion Sci. Technol.*, 2020, **41**, 690–698.
38 G. Lawrie, I. Keen, B. Drew, A. Chandler-Temple, L. Rintoul, P. Fredericks and L. Grøndahl, *Biomacromolecules*, 2007, **8**, 2533–2541.
39 G. Nikolic, S. Zlatkovic, M. Cakic, S. Cakic, C. Lacnjevac and Z. Rajic, *Sensors*, 2010, **10**, 684–696.
40 G. Tripodo, A. Trapani, A. Rosato, C. Di Franco, R. Tamma, G. Trapani, D. Ribatti and D. Mandracchia, *Carbohydr. Polym.*, 2018, **198**, 124–130.
41 A. Othmani, M. Derbali, R. Kalfat, F. Touati and H. Dhaouadi, *J. Mater. Res. Technol.*, 2021, **15**, 5762–5775.
42 S. V. Prabhakar Vattikuti, A. K. R. Police, J. Shim and C. Byon, *Sci. Rep.*, 2018, **8**, 4194.
43 N. Kuş, S. H. Bayari and R. Fausto, *Tetrahedron*, 2009, **65**, 9719–9727.
44 N. Sakthiguru and M. A. Sithique, *Int. J. Biol. Macromol.*, 2020, **152**, 873–883.
45 Y. D. Nokoorani, A. Shamloo, M. Bahadoran and H. Moravvej, *Sci. Rep.*, 2021, **11**, 16164.
46 M. Li, J. Chen, M. Shi, H. Zhang, P. X. Ma and B. Guo, *Chem. Eng. J.*, 2019, **375**, 121999.
47 B. Zhang, J. He, M. Shi, Y. Liang and B. Guo, *Chem. Eng. J.*, 2020, **400**, 125994.
48 X. Dong, J. Ye, Y. Chen, T. Tanziela, H. Jiang and X. Wang, *Chem. Eng. J.*, 2021, **432**, 134061.
49 O. Sarheed, A. Ahmed, D. Shouqair and J. Boateng, *Wound Healing – New insights into Ancient Challenges*, 2016.
50 X. Li, H. Bai, Y. Yang, J. Yoon, S. Wang and X. Zhang, *Adv. Mater.*, 2019, **31**, 1805092.

51 L. Wang, X. Zhang, K. Yang, Y. V. Fu, T. Xu, S. Li, D. Zhang, L. N. Wang and C. S. Lee, *Adv. Funct. Mater.*, 2020, **30**, 1904156.
52 E. Niza, C. Nieto-Jiménez, M. D. M. Noblejas-López, I. Bravo, J. A. Castro-Osma, F. de la Cruz-Martínez, M. M. D. S. Buchaca, I. Posadas, J. Canales-Vázquez, A. Lara-Sanchez, D. Hermida-Merino, E. Solano, A. Ocaña and C. Alonso-Moreno, *Nanomaterials*, 2019, **19**, 1208.
53 G. Broughton, J. E. Janis and C. E. Attinger, *Plast. Reconstr. Surg.*, 2006, **117**, 12S–34S.
54 J. R. Davidson, *Vet. Clin. North Am. Small Anim. Pract.*, 2015, **45**, 537–564.
55 M. Kaushik, R. Niranjan, R. Thangam, B. Madhan, V. Pandiyarasan, C. Ramachandran, D. H. Oh and G. D. Venkatasubbu, *Appl. Surf. Sci.*, 2019, **479**, 1169–1177.
56 X. Zhang, B. Tan, Y. Wu, M. Zhang, X. Xie and J. Liao, *Carbohydr. Polym.*, 2022, **293**, 119722.
57 Z. Zhou, Z. Chen, C. Ji, C. Wu, J. Li, Y. Ma, S. Jin, X. Fang, Y. Wu, J. Xun, S. Xiao, S. Wang and Y. Zheng, *Chem. Eng. J.*, 2024, **498**, 155389.

